Biosensors and Bioelectronics 192 (2021) 113490

Contents lists available at ScienceDirect

Biosensors and Bioelectronics

journal homepage: www.elsevier.com/locate/bios

Alloyed AuPt nanoframes loaded on h-BN nanosheets as an ingenious ultrasensitive near-infrared photoelectrochemical biosensor for accurate monitoring glucose in human tears

Yue Tian [a,b], Qingqiang Cui [a], Linlin Xu [a], Anxin Jiao [a], Hui Ma [a], Chang Wang [a], Mengya Zhang [a], Xuelin Wang [b], Shuang Li [c,**], Ming Chen [a,*]

[a] School of Physics, Shandong University, Jinan, 250100, China
[b] Institute of Frontier and Interdisciplinary Science, Shandong University, Qingdao, 266237, China
[c] School of Science, Shandong Jianzhu University, Jinan, 250101, China

ARTICLE INFO

Keywords:
Near infrared photo-electro-chemical biosensor
h-BN/Au_5Pt_9 nanoframes
Tear glucose
Localized surface plasmon resonance

ABSTRACT

Photo-electro-chemical (PEC) glucose biosensor has recently attracted extensive attention due to the double advantages of both photocatalysis via photon energy utilization and electrocatalytic oxidation through extra electric field. Compared with previous shorter wavelength (violet-visible) light-induced PEC reaction, the anticipated near infrared (NIR, >~700 nm) excited PEC biosensor with multiple fascinating features should be more suitable for clinical diagnostic biology. Herein, we report an ingenious NIR-PEC biosensor by loading alloyed Au_5Pt_9 nanoframes on two dimensional (2D) hexagonal boron nitride (h-BN) nanosheets. The obtained h-BN/Au_5Pt_9 nanoframes exhibit a remarkable higher NIR-PEC activity in comparison with other as-prepared h-BN/AuPt references. The improved PEC performance is attributed to the enhanced synergetic coupling effect between Au_5Pt_9 nanoalloys and constitutionally stable h-BN that gives rise to a stronger absorbance capacity and pronounced localized surface plasmon resonance (LSPR) in visible-NIR region as well as high free-electron mobility of framework-like Au/Pt. Interestingly, the obtained h-BN/Au_5Pt_9 nanoframes excited by 808 nm NIR light provide superior PEC accuracy and sensitivity as compared to visible or other NIR light irradiation. Then, the novel 808 nm NIR-PEC biosensor was used for precise glucose monitoring in human tears with a detectable concentration of 0.03~100 μM and a low detection limit of 0.406 nM. Undoubtedly, the proposed h-BN/Au_5Pt_9 nanoframes as an appealing NIR-PEC glucose biosensor can possess greater potential values for practical glucose monitoring in biomedicine.

1. Introduction

Glucose biosensors have attracted extensive research due to their potential application in clinical diagnostic biology, fuel cell, biotechnology and food monitoring, *etc.* (Yoo et al., 2010; Basu et al., 2010; Barman et al., 2012; Adriaenssens et al., 2019). Especially, the highly sensitive biosensors with rapid response and excellent reliability, can realize the precise assessment of glucose concentration in human body, playing a critical role in the diagnosis and treatment of diabetes mellitus (DM) (Kownacka et al., 2018; Salsali and Nathan, 2006; Han et al., 2020). Some alternative glucose biosensors based on saliva (Arakawa et al., 2016), sweat (Han et al., 2020; Toi et al., 2019), tear (Romeo et al., 2018; Yao et al., 2011) and urine (Karim et al., 2018) have recently garnered considerable interest, since they can effectively reduce inconveniences during the invasive method of blood sampling with needle bleeding. In particular, glucose monitoring in tear fluid with a typical glucose range of around 0.1–0.6 mM (Yao et al., 2011) has been regarded as an appealing way to indirectly reflect the situation of blood glucose. Up to now, numerous glucose detection techniques were already proposed, such as electrochemistry, chemiluminescence, spectrophotometry and colorimetry, *etc.* (Wang, 2008; Li et al., 2017; Yamakoshi et al., 2006; Huang et al., 2016). Especially, the electrochemical sensing can be served as one of the most promising methods owing to fast response, high stability, sensitivity, repeatability, high

* Corresponding author.
** Corresponding author.
E-mail addresses: lishuang@sdjzu.edu.cn (S. Li), chenming@sdu.edu.cn (M. Chen).

https://doi.org/10.1016/j.bios.2021.113490
Received 30 April 2021; Received in revised form 24 June 2021; Accepted 6 July 2021
Available online 9 July 2021

precision, low power consumption and cost-effectiveness (Chen et al., 2020; Chiu et al., 2020; Nantaphol et al., 2017). Besides the electrocatalysis, the oxidation of glucose molecules through photocatalysis is also a feasible method, which is usually applied in the field of photon energy conversion (Madriz et al., 2020; Zhou et al., 2016; Iervolino et al., 2018). Therefore, the novel photo-electro-chemical (PEC) reaction can simultaneously take advantage of both photocatalytic reaction via the utilization of photon energy and the electrocatalytic oxidation through extra electric field (Yang et al., 2020; Wang et al., 2017; Li et al., 2012). Compared to the mere electrochemical or photocatalytic technique, the ingenious PEC biosensor can possess higher applicability for ultrasensitive glucose monitoring in diverse fields.

As for the PEC biosensor, it should not only exhibit superior electrocatalytic performance towards the reactions occurring at both anode and cathode, but also have the effective plasmonic effect with the high capacity of harvesting light in the broad wavelength range to induce the oscillation charge carriers (Li et al., 2021; Chao et al., 2019; Linic et al., 2015). In this way, plasmonic Au-based nanocomposites (NCs) have been frequently used in direct plasmon-accelerated electro-oxidation and constructed a plasmon-improved glucose electrochemical sensor (Wang et al., 2017, 2019). For instance, Au/NiAu multilayered nanowire (Wang et al., 2018) and AuNi nanodendrite arrays (Wang et al., 2019) as well as the Au–NiO_{1-x} ($0 < x < 1$) hybrid nanowire (Wang et al., 2020) were proposed as novel plasmon aided non-enzymatic glucose biosensors. In addition, the local surface enhanced resonance (LSPR) of Au NCs can still be stimulated by monochrome blue or green LED illumination, improving the sensitivity of glucose biosensor (Hsu et al., 2017). On the other hand, despite numerous great achievements in the construction of PEC biosensors, there is still an urgent issue to be considered in this field. Most of pervious works merely focused on the shorter wavelength (violet-visible) light-accelerated PEC glucose monitoring, while the near infrared (NIR) light is seldomly involved in PEC biosensors. The main reason is that the simple and discontinuous Au nanoparticles (NPs) with inherent LSPR peak at ~520 nm are usually adopted in glucose biosensors, determining the PEC reactions were restricted to violet-visible light excitation with higher photon energy. It is well known that the excellent NIR response-harvest-conversion can be effectively realized by construction of diverse anisotropic Au-based nanostructures (nanorods (Yoshii et al., 2019; Yoshii et al., 2021), nanostars (Peng et al., 2018), nanoporous (Lu et al., 2018), nanodendrites (Wang et al., 2019), *etc.*). Compared with ultraviolet or visible light, the NIR light that accounts for over 50% of solar energy (Liu et al., 2019) can be served as a biological tissue optical window, reaching a maximum depth in biological tissue with low photo-damage and having minimum interference from background autofluorescence in living biosystems (Cao et al., 2020; Liu et al., 2020). Therefore, superior to shorter wavelength excitation, the anticipated NIR-PEC glucose biosensor with multiple fascinating features is more suitable for practical glucose monitoring in diagnose, surgery and therapy.

Herein, we rationally proposed an appealing NIR-PEC glucose biosensor by loading alloyed Pt/Au nanoframes on 2D h-BN nanosheets, which can be effectively used to achieve broadband light response-harvest-conversion from visible to NIR region. Obviously, the obtained h-BN/Au_5Pt_9 nanoproducts with Au/Pt ratio of 5/9 after appropriate annealing at 200 °C for 2 h possess a remarkable higher PEC activity under visible-NIR light excitation, as compared to the other as-prepared h-BN/AuPt references. Adopting 808 nm NIR excitation, the optimal h-BN/Au_5Pt_9 nanoframes served as a novel NIR-PEC biosensor can provide accurate and ultrasensitive glucose monitoring of human tears, reaching a detection concentration range of 0.03–100 μM and a low detection limit of 0.406 nM. The corresponding schematic diagram was shown in Scheme S1 in Supporting Information (SI). Moreover, the excellent selectivity, reproductivity and long-term stability of h-BN/Au_5Pt_9-based NIR-PEC glucose biosensor will be favorable for ultrasensitive NIR-PEC glucose monitoring of clinical diagnostics in the near future.

2. Experimental setup

The experimental chemicals, characterization and experimental methods are provided in SI.

3. Results and discussion

3.1. Characterization of h-BN/AuPt NCs

The h-BN/Pt (Section S1 in SI) can be used as the precursors for overgrowth of bimetallic Pt/Au core-shell structure via the galvanic replacement reaction. Then, the structural characterizations of the obtained h-BN/Pt/Au are measured by transmission electron microscopy (TEM) in Fig. 1(a). The Pt/Au on h-BN supports have obvious solid cores with darker contrasting light images and thick shell architectures, which are randomly bonded to each other on the 2D surfaces. Besides the fringe distance of 0.332 nm assigned to the h-BN (002) plane (Fig. 1(b)), the inner core with 0.237 nm is related to Pt (111), and another lattice fringe of 0.236 nm on the shell is located between the theoretical values of (111) lattice plane of Au (0.235 nm) and Pt (0.237 nm). In Fig. 1(c) and 1 (d), after annealing at 200 °C for 2 h, the AuPt NPs are connected to each other, forming a framework-like structure on the 2D h-BN nanosheet, indicating that appropriate annealing has the potential to reshape the microstructure of bimetallic Au/Pt through the interdiffusion process in thermal environment. On the other hand, the framework-like structure cannot be formed in the absence of h-BN supports, as the aggregated NPs shown in Fig. S2. Moreover, the high-resolution TEM (HRTEM) images (Fig. 1(e)) illustrate that lattice fringes of ~0.236 nm correspond to the formation of alloyed AuPt nanocrystals. The intuitive elemental mapping images in Fig. 1(f) also verify the structure of the alloyed AuPt nanoframes on 2D h-BN supports. The interconnected distribution of Au and Pt elements is accompanied by the uniform B and N elements throughout the whole nanosheet. The atomic ratio of Au to Pt species is about 6.3:11.2, reaching the approximate value of 5:9, which is also close to the result of 3.1:5.5 obtained by energy-dispersive X-ray spectroscopy (EDS) pattern (Fig. S3(a)). Therefore, the obtained h-BN/AuPt nanoframes are abbreviated to be h-BN/Au_5Pt_9 in this paper, and the subscript indicates the relative molar ratio of Au to Pt in the NCs. On the other hand, the h-BN/AuPt nanoalloys with different bimetallic compositions have also prepared as reference samples (EDS patterns illustrated in Section S2 in SI). Additionally, the surface compositions and chemical states of these different nanohybrids were further evaluated by X-ray photoelectron spectroscopy (XPS) analyses, optimizing the Au/Pt ratio to achieve enhanced catalysis (Section S3, S4 in SI).

3.2. Condition optimization of h-BN/AuPt NCs

The spatial distribution of metallic atoms via interdiffusion process in a heated environment will also provide another contribution for further improving coupling synergy of h-BN/Au_5Pt_9 NCs. As the high-resolution XPS patterns shown in Fig. 2(a), compared with the Pt^0 $4f_{7/2}$ binding energy derived from unannealed h-BN/Au_5Pt_9 NCs (70.5 eV), the position exhibits a gradual negative-shift and turns into 70.4 and 70.3 eV by using 100 and 200 °C heated temperatures, respectively. Further increasing annealing temperature (>200 °C), the peak positions of Pt^0 $4f_{7/2}$ have a reverse trend. Additionally, the XPS peak position of Au^0 $4f_{7/2}$ is 83.8 eV after 200 °C annealing treatment in Fig. 2(b), suggesting the formation of ~0.2 eV positive-shift with respect to unannealed one. A remarkable negative shift of Pt^0 $4f_{7/2}$ and a positive shift of Au^0 $4f_{7/2}$ are observed simultaneously for the annealed h-BN/Au_5Pt_9 via 200 °C temperature, owing to the electron transfer from Au to Pt atoms by atomic diffusion at the interfaces (Peng et al., 2018; Li et al., 2016). Additionally, the XRD patterns of the bimetallic AuPt samples show that the four peaks at 39.6, 45.9, 67.1, 80.9 and 85.3° are between pure Pt and Au (JCPDS, no. 04-0802 and JCPDS, no. 04-0784). The full width at half maximum (FWHM) of diffraction peak is obviously

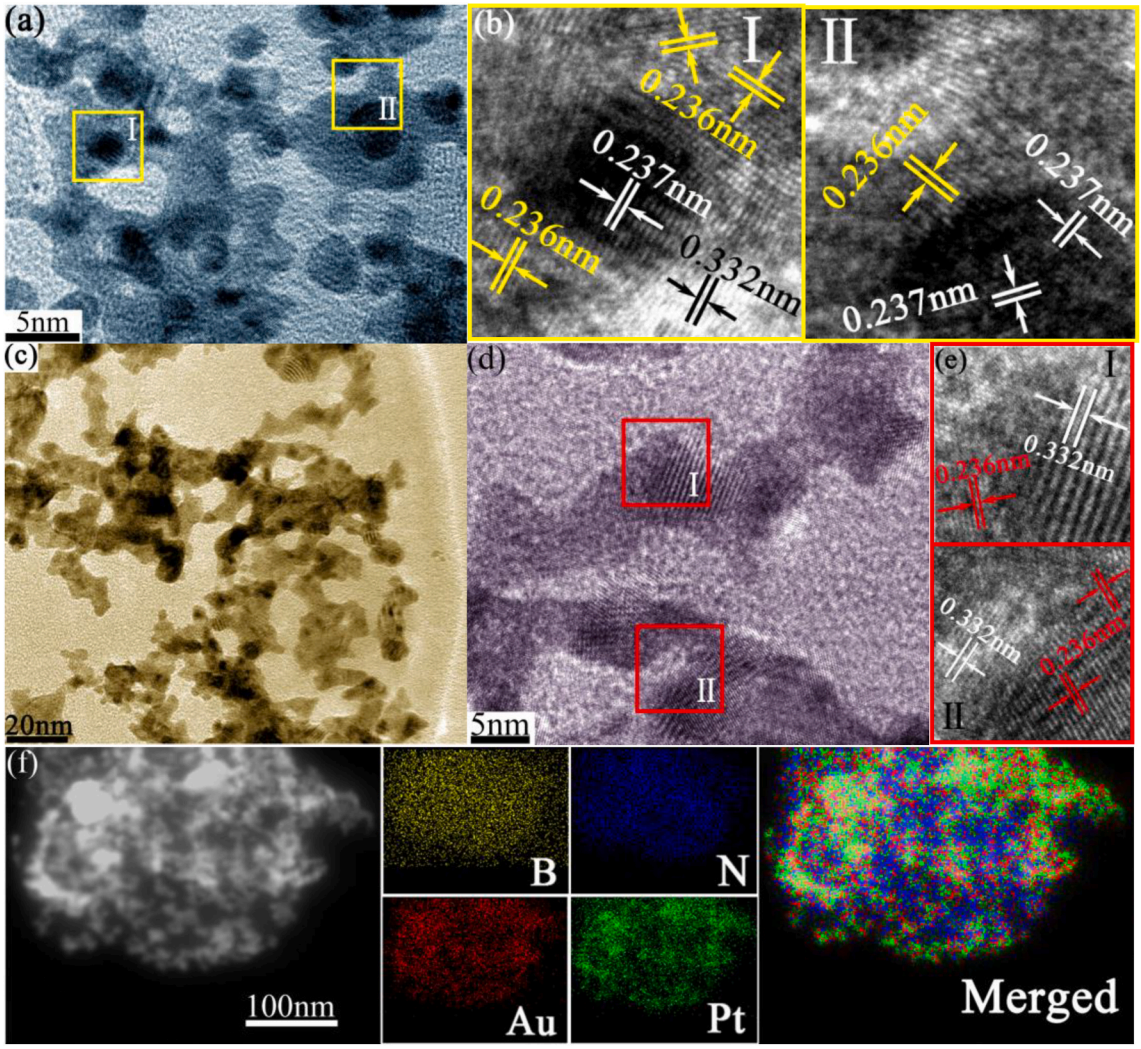

Fig. 1. Morphology and structural characterizations of the obtained h-BN/Au_5Pt_9 before and after 200 °C annealing. (a) TEM and (b) HRTEM images of unannealed h-BN/Au_5Pt_9 NCs. (c–d) TEM, (e) HRTEM and (f) element mapping images of a piece of h-BN/Au_5Pt_9 nanoframes.

decreased with an increase of annealing temperature. As for (111) plane at 39.6°, the values of FWHM are calculated about 1.74 for unannealed NCs, 1.39 and 0.97 for 100 °C and 200 °C annealing, respectively. It indicates that the core-shell structure is transformed into a uniform alloy structure (He et al., 2008; Csapó et al., 2012). Furthermore, the absorption spectra of h-BN/AuPt NCs via annealing treatment with different temperatures are shown in Fig. 2(d). Clearly, the appropriate annealing treatment at 200 °C can enable the light-harvesting efficiency of h-BN/AuPt NCs to be obviously broadened and enhanced in visible-NIR region (400~1100 nm), which is closely related to the Au_5Pt_9 alloyed frame-like structures (Fig. 1(c)–1(f)). These results imply that the LSPR property of the alloyed h-BN/Au_5Pt_9 nanoframes can be significantly improved by the annealing treatment at appropriate temperature of 200 °C, holding great potential for promoting their photo-assisted catalytic performance.

3.3. PEC enhancement mechanism

Then, the corresponding methanol oxidation reaction (MOR) electrocatalytic performance of h-BN/Au_5Pt_9 nanoframes was performed. For comparison, the reference samples annealed at 100 °C, 300 °C and 400 °C and the unannealed one were also adopted. In Fig. 3(a) and (b), the mass activity of h-BN/Au_5Pt_9 nanoframes is measured about 500.7 mA mg_{Pt}^{-1} and much higher than other four reference samples. Moreover, the CV measurements of h-BN/Au_5Pt_9 nanoframes and four reference samples are illustrated by laser irradiations (532, 635, 808 and 980 nm) (Fig. 3(c)–3(f), Fig. S8). Compared with the dark condition, the oxidation current densities increased under excitation with different-wavelength lasers in varying degrees. Furthermore, the xenon lamp with most of the visible-NIR lights can further improve the MOR. Then, the mass activities of the five nanocatalysts as a function of the incident source wavelength are separately plotted in Fig. 3(d) and (f), S7(b), S7 (d) and S7(f). Interestingly, as for the h-BN/Au_5Pt_9 nanoframes (inset in Fig. 3(f)), the mass activity in Fig. 3(e) can be simultaneously enhanced by 532, 635, 808 or 980 nm irradiation, which is 1.51, 1.60, 1.45 and 1.33 times higher than that under dark condition. In Fig. 3(f), the improved catalytic activity can be well maintained by changing the visible light excitation (532 or 635 nm) to NIR (808 or 980 nm) irradiation, which is agree with the broader range of absorption band across visible and NIR range. Adopting xenon lamp with full visible-NIR lights as an irradiation source can further achieve a maximum mass activity of 941.9 mA mg_{Pt}^{-1}, which is 8.42 and 3.93 times higher than that of h-BN/Pt and Pt/C (Fig. S7(a)). Compared to the h-BN/Au_5Pt_9 nanoframes, the catalytic deactivation of reference samples generated by overheating temperature (>200 °C in Fig. S8(c)–S8(f)) is related to that the framework-like structure of Au_5Pt_9 nanoalloys can be destroyed under excessive high temperature. In summary, despite the five samples with same bimetallic Au_5Pt_9 composition, the alloyed h-BN/Au_5Pt_9

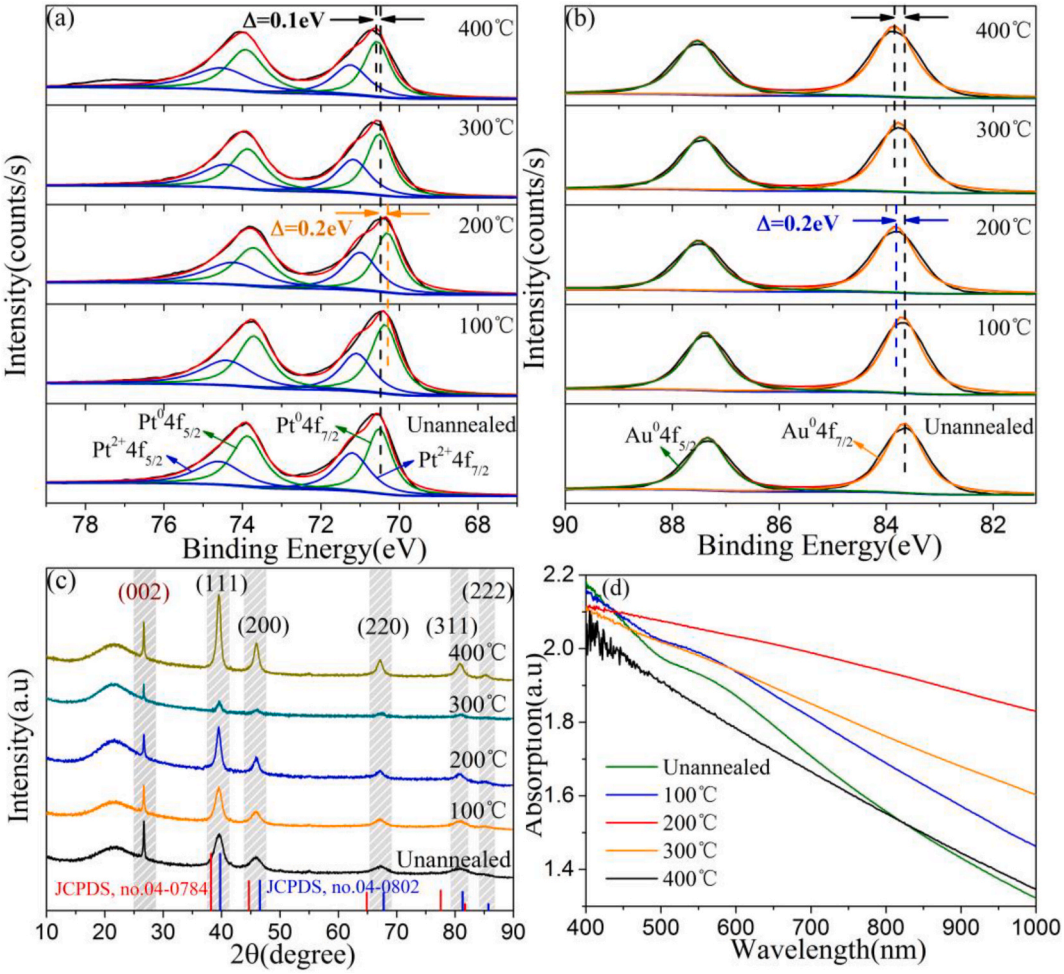

Fig. 2. XPS spectra of metallic (a) Pt and (b) Au and (c) XRD results and (d) UV-visible absorption spectra of h-BN/Au_5Pt_9 NCs at different annealing temperatures.

nanoframes possess an enhanced catalytic activity in comparison with discontinuous NPs on h-BN.

Then, the transient photocurrent responses of h-BN/Au_5Pt_9 nanoframes via different wavelength lasers irradiation on and off were separately performed in Fig. 4(a). The enhanced current density upon visible or NIR laser irradiation indicates that more electrons are supplied to the external circuit. It may stem from the separation of hot electrons and hot holes on the Au surface upon photo-excited collective oscillation of electrons due to the existence of strong plasmonic effect (Wang et al., 2018), leading to rapid injection of hot electrons from Au to external circuit at a constant bias potential (Wang et al., 2017). Meanwhile, the degree of photocurrent enhancement is highly dependent on the incident excitation wavelength (Fig. S9). When 0.5 M methanol is injected into the electrolyte, a sharp increase in photocurrent is detected upon LSPR excitation, and the photocurrent drops precipitously as soon as the irradiated light is switched off. The methanol molecules that are acted as the scavengers of energetic holes generated by photo-excitation will suppress the recombination of hot electron-hole pairs on metallic surfaces, prompting the transmission of photo-excited electrons. Additionally, large quantities of small-sized hydroxyl anions (OH^-) can diffuse to the surfaces of nanocatalysts in highly alkaline environment (Wang et al., 2017), which will be oxidized into numerous hydroxyl radicals ($^{\bullet}OH$) radicals due to the high oxidation capability of photon-excited hot holes. In this manner, plentiful $^{\bullet}OH$ radicals can quickly diffuse into the solution to realize the oxidation of methanol, facilitating the catalytic oxidation activity. At the same time, taking advantage of the interconnected framework-like structure of Au_5Pt_9 nanoalloys on h-BN, the hot electrons can be effectively delivered to external circuits without delay, giving rise to the enhanced photocurrent response under visible-NIR irradiation. Furthermore, compared with the unannealed NCs (Fig. 4(b)), the h-BN/Au_5Pt_9 nanoframes have a lower impedance under visible-NIR light irradiation, demonstrating its excellent mass transfer and electron transfer kinetics in the electrocatalytic process (Chen et al., 2020). This obvious reduction of charge transfer impedance is attributed to the unique framework structure of the hybrid and the LSPR effect of Au in visible-NIR region. In addition, stability is another key parameter for evaluating the electrocatalytic performance, which is generally affected by the deactivation sites via the accumulation of carbonaceous intermediates formed during electrocatalysis (Wang et al., 2014). As displayed in Fig. 4(c), the i-t curves of catalytic activity as a function of reaction time were separately investigated upon different light irradiations, suggesting the excellent stable current densities derived from visible 635 nm or NIR 808 nm irradiation. In addition, it is worth noting that photo-excitation is helpful to extract photoinduced electrons from Au and transfer to Pt. Thus, it will lead to a self-photo-reduction process and more regenerative Pt active sites ($PtO_x + e^- \rightarrow Pt$) (Xie et al., 2020) and improve the long-term durability of the catalyst. The corresponding MOR process upon LSPR excitation is exhibited in Fig. 4(d). Meanwhile, the continued irradiation by xenon lamp enables the current density to slightly increase in Fig. 4(c), which is likely attributed to the plasmon-enhanced localized photothermal effect (Section S7 in SI).

3.4. Glucose detection

Then, the PEC sensitivity of h-BN/Au_5Pt_9 nanoframes was illustrated

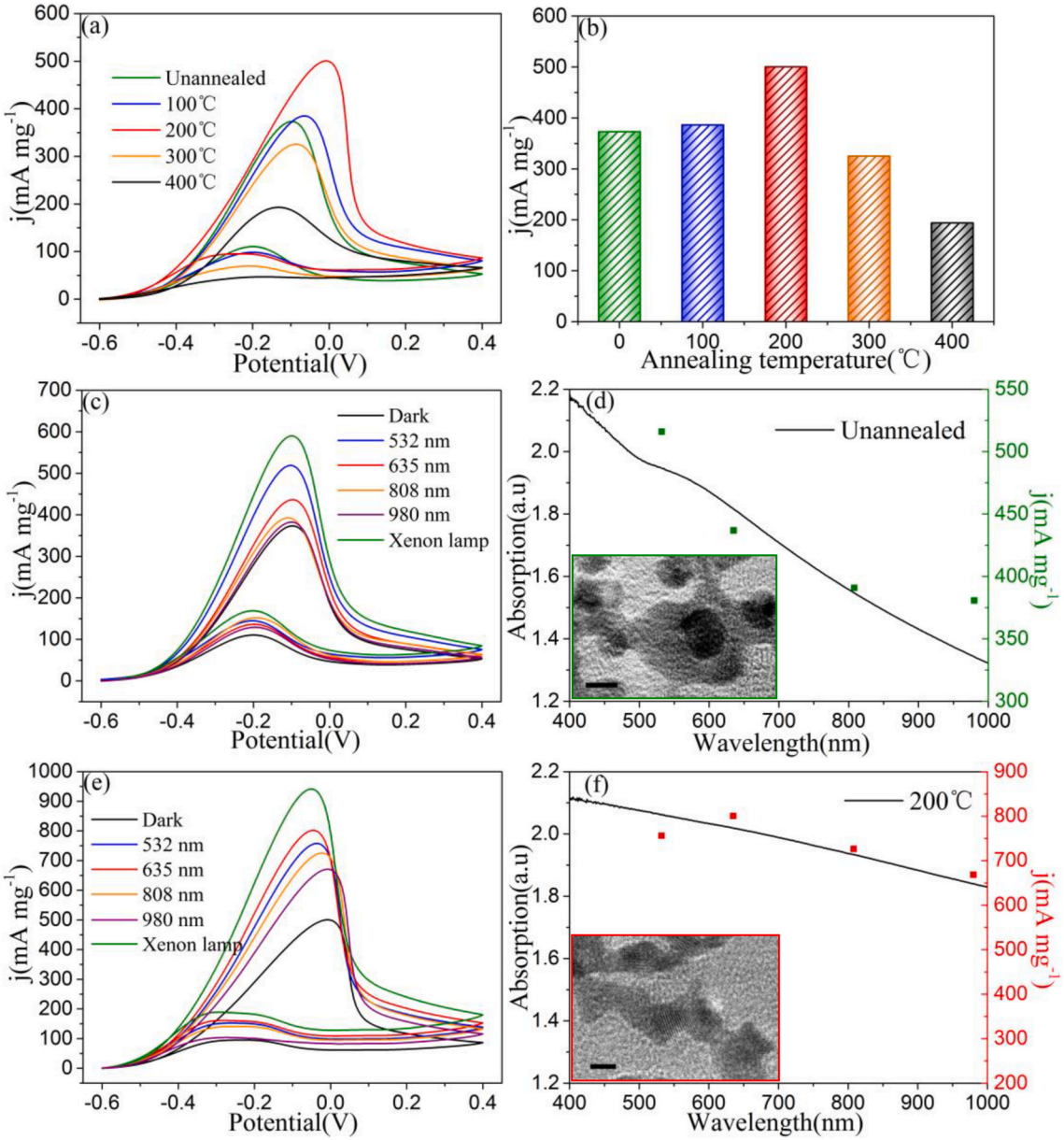

Fig. 3. (a) CV curves and (b) the corresponding peak current densities of h-BN/Au_5Pt_9 NCs at different annealing temperatures in the dark. The CV responses of h-BN/Au_5Pt_9 NCs at different excitation wavelengths with (c) unannealed treatment and (e) annealing at 200 °C. (d) and (f) The UV-visible absorption spectra of catalysts at different annealing temperatures. Overlaid dots are mass activities of catalysts as a function of the laser wavelength.

by differential pulse voltammetry (DPV) tests. The oxidation current at 0.31 V in the dark condition (Fig. 5(a)) gradually increases with the increase of glucose concentration from 0 to 1 mM, confirming the intrinsic glucose electrocatalytic oxidation behavior of h-BN/Au_5Pt_9 nanoframes (Nantaphol et al., 2017; Koskun et al., 2018). Considering the sensitive light response of the unique h-BN/Au_5Pt_9 nanoframes with pronounced visible-NIR LSPR property as discussed above, the sensitivity of glucose biosensor can be further improved by light assistance with glucose molecules acting as effective scavengers of photon-excited hot holes (Girardi et al., 2019). Compared to the dark condition, the amperometric response of glucose biosensor can be significantly improved with the aid of visible (532, 635 nm) or NIR (808, 980 nm) excitation, in Fig. 5(b). It is illustrated that their enhanced response upon visible-NIR light excitation is highly correlated with broader LSPR property of h-BN/Au_5Pt_9 nanoframes. Then, the calibration curves of these current intensities versus the relevant glucose concentrations are plotted in Fig. 5(c) and the corresponding linear regression equations are summarized in Fig. 5(d). It is concluded that the h-BN/Au_5Pt_9 nanoframes excited by NIR lights (808 nm and 980 nm) give rise to better R^2 values at both two linear regions (0.1–1.0 mM and 1.0–17 mM), which is more conducive to improve the accuracy of the glucose sensor. Additionally, in the range of 0.1–1.0 mM, the sensitivities of glucose biosensor excited by 808 and 980 nm are calculated about 338.63 and 243.16 μA mM^{-1} cm^{-2}, and 79.89 and 72.81 μA mM^{-1} cm^{-2} in the range of 1.0–17 mM, respectively (Fig. 5(d)). Thus, the 808 nm light can possess a higher PEC sensitivity in comparison with 980 nm excitation, especially for ultralow (<1.0 mM) glucose monitoring. Therefore, the 808 nm NIR-PEC glucose biosensor based on alloyed h-BN/Au_5Pt_9 nanoframes is preferentially considered in this work. Under 808 nm excitation, the h-BN/Au_5Pt_9 nanoframes can also exhibit a better photocurrent response than that of h-BN/Au, h-BN/Pt or bimetallic Au_5Pt_9 NCs, as shown in Fig. S11. Additionally, the glucose concentrations were further narrowed and the amperometric responses of this 808 nm NIR-PEC biosensor in the range of 0.03–100 μM (Fig. 5

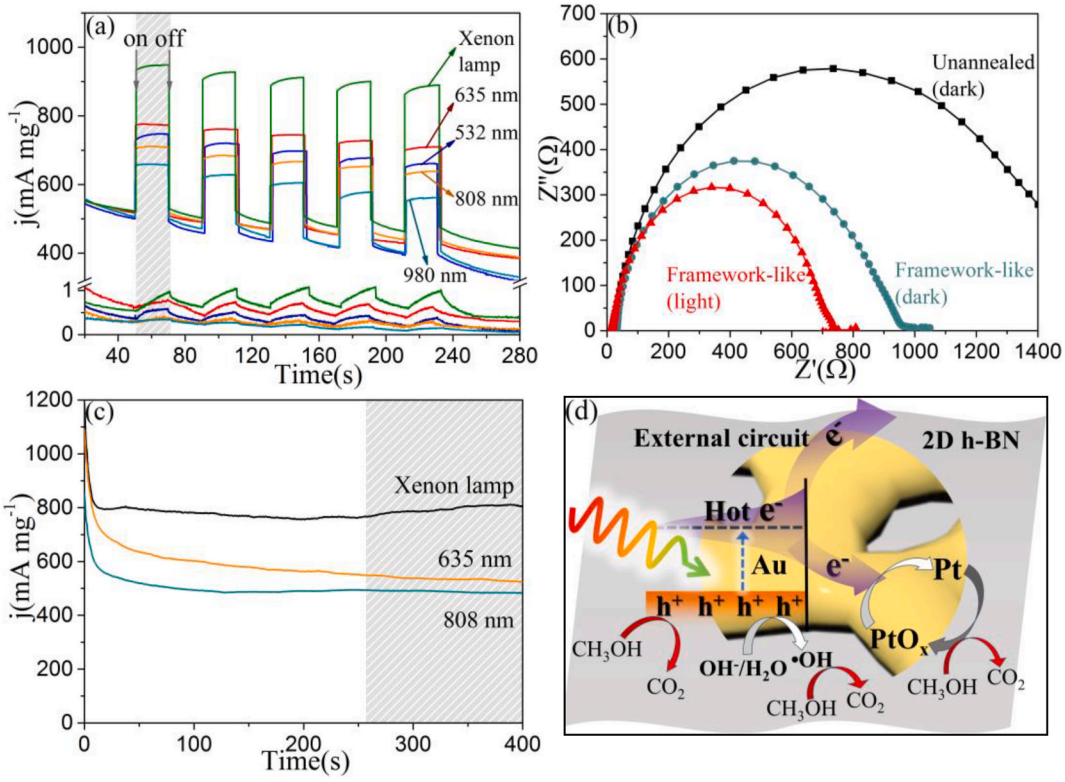

Fig. 4. (a) Transient photocurrent responses of h-BN/Au_5Pt_9 nanoframes in 1 M KOH in the absence (at the bottom) and presence of 0.5 M CH_3OH (the upper part). (b) Nyquist plots of the h-BN/Au_5Pt_9 nanoframes with xenon lamp switching on and off as well as the unannealed NCs in MOR. (c) I–t curves for h-BN/Au_5Pt_9 nanoframes under illumination in MOR. (d) Schematic of the surfaces of Pt and Au excited by LSPR in MOR.

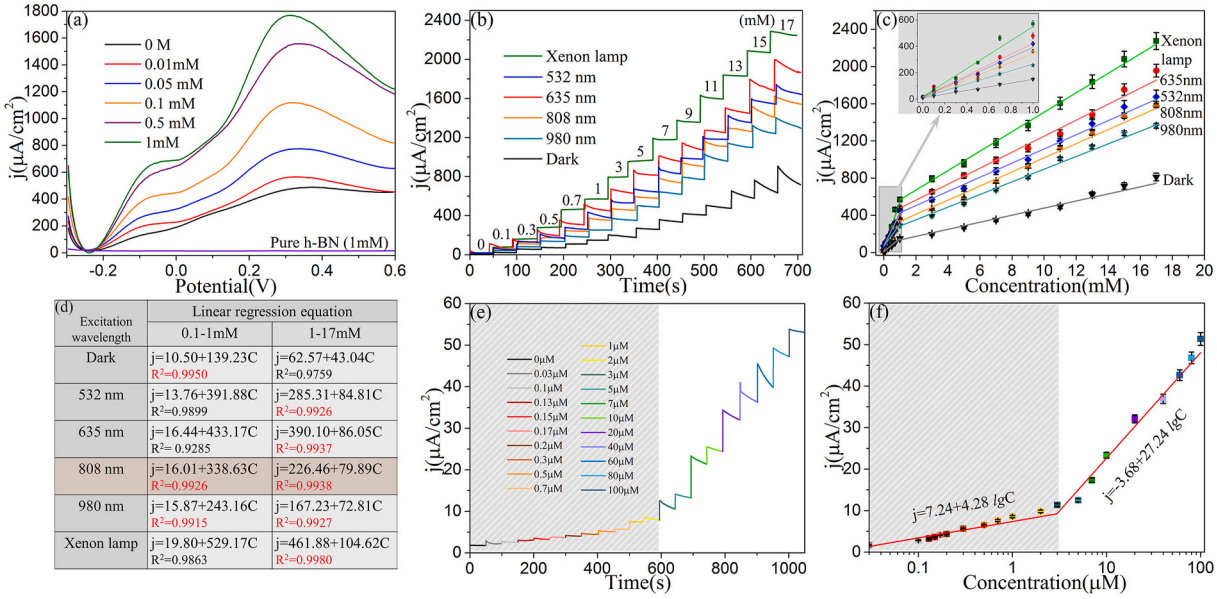

(d)

Excitation wavelength	Linear regression equation	
	0.1-1mM	1-17mM
Dark	j=10.50+139.23C R^2=0.9950	j=62.57+43.04C R^2=0.9759
532 nm	j=13.76+391.88C R^2=0.9899	j=285.31+84.81C R^2=0.9926
635 nm	j=16.44+433.17C R^2= 0.9285	j=390.10+86.05C R^2=0.9937
808 nm	j=16.01+338.63C R^2=0.9926	j=226.46+79.89C R^2=0.9938
980 nm	j=15.87+243.16C R^2=0.9915	j=167.23+72.81C R^2=0.9927
Xenon lamp	j=19.80+529.17C R^2=0.9863	j=461.88+104.62C R^2=0.9980

Fig. 5. (a) DPV curves of the h-BN/Au_5Pt_9 nanoframes electrode in the dark in 0.1 M PBS (pH 7.34), containing different concentrations of glucose (0, 0.01–1 mM) in artificial tears. (b) Amperometric responses, (c) calibration plot and (d) corresponding linear regression equations obtained by using h-BN/Au_5Pt_9 nanoframes in artificial tear containing different concentrations of glucose (100–17000 μM) with or without LSPR excitation. (e) Amperometric responses and (f) linear regression equations with excitation of 808 nm in 0.1 M PBS containing artificial tears with different concentrations of glucose (0, 0.03–100 μM). All of the applied potential is 0.31 V.

(e)). In Fig. 5(f), the glucose detection sensitivities in ultralow concentration range (0.03–2.99 μM) and low concentration range (2.99–100 μM) are calculated about 4.28 and 27.24 $\mu A(lg\mu M)^{-1}cm^{-2}$, respectively. The detectable limit is calculated to be 4.06 nM, according to the formula LOD = 3σ/*s* (Han et al., 2020) (σ is the standard deviation of the blank signal (n = 5, shown in Fig. S12) and s is sensitivity of the sensor). It is better than many pervious results based on single electrocatalytic reactions or visible light-assisted catalytic reactions (Wang et al., 2018,

2019; Toi et al., 2019; Chiu et al., 2020; Jia et al., 2016; Grochowska et al., 2017; Yang et al., 2017; Koskun et al., 2018). Moreover, some coexisting species, such as some inorganic salts, urea and ascorbic acid (AA), may interfere with the sensitivity of glucose biosensor (Yang et al., 2017). Then, the response currents were measured by adding 0.25 μM glucose and 0.1 mM KCl, $CaCl_2$, NaCl, urea and AA to evaluate the selectivity of the 808 nm NIR-PEC biosensor (Fig. S13). There is only a negligible fluctuation after the injection of these interfering substances. Meanwhile, some other interfering species such as lactose, sucrose, L-cysteine, ethanol and methanol molecules that work as hot hole scavengers will give to some slight fluctuations of current responses in Fig. S14. Then, the long-term stability of this NIR-PEC biosensor was performed within a long-time period of 20 days. The corresponding current response (Fig. S15(a)) can be well maintained after 20 days and the last recorded current still remained at 96.7% of the initial value. Meanwhile, TEM image of the used sample (Fig. S15(b)) maintains the identical morphology with well-defined framework-like nanostructures. Moreover, the reproducibility was evaluated by six identical independently h-BN/Au_5Pt_9 nanoframes (Fig. S15(c)). The amperometric current response can be well repeated upon different samples, and the relative standard deviation (RSD) is calculated no more than 5%.

Finally, the established biosensor was applied to the sensitive monitoring of glucose level in actual tears. Under 808 nm NIR excitation, the amperometric response curves of the diluted tears in PBS from five different volunteers (included a 15-year-old girl, a 17-year-old boy, a 40-year-old woman, a 43-year-old man and a 65-year-old woman) were performed. The recovery values gathered in Fig. S16 are calculated about 108.8%, 101.3% and 94.5%, respectively (Table S1), in the range of 90%–110%, indicating the biosensor is accurate for practical clinical diagnosis. Then, the calculated actual glucose concentrations of different volunteers' tear are illustrated in Fig. 6(b). Additionally, as a reference, the blood glucose levels of these volunteers were recorded with a commercial blood glucose meter. The glucose concentrations of tears and blood sugar are plotted in Fig. 6(c), suggesting that a high correlation between tear glucose and blood sugar does exist. Meanwhile, it should be noted that the precise monitoring of individual glucose fluctuation in daily life is also a critical indicator for assessing many metabolic diseases. Therefore, in Fig. 6(d)–6(e), the as-prepared NIR-PEC biosensor was further used to monitor the glucose fluctuation in tears of a volunteer before and after breakfast (or dinner). The glucose levels of this volunteer increased significantly after a meal. Interestingly, the different increases in glucose levels caused by eating different foods for breakfast or dinner can also be distinguished by this ultrasensitive NIR-PEC biosensor, which were also comparable to the results of commercial blood glucose-meter (Fig. 6(f)). Undoubtedly, the unique NIR-PEC biosensor based on alloyed h-BN/Au_5Pt_9 nanoframes possesses high applicability in ultrasensitive glucose monitoring of body fluids.

4. Conclusion

An interesting NIR-PEC biosensor based on alloyed h-BN/Au_5Pt_9 nanoframes has been established for ultrasensitive glucose monitoring in human tears. The h-BN/Au_5Pt_9 nanoframes with enhanced intermetallic synergetic effect provide a significantly improved electrocatalytic performance. Moreover, the uniform alloyed framework-like feature enables the h-BN/Au_5Pt_9 nanoframes to exhibit a broader and stronger absorption across visible-NIR region, which can further improve the catalytic activity upon LSPR excitation (400–1000 nm). Interestingly, it is proved that the 808 nm NIR excitation is conducive to exhibit higher PEC accuracy and sensitivity for ultralow glucose monitoring, in comparison with visible or other NIR lights. Finally, the 808 nm NIR-PEC glucose biosensor is applied to monitor the glucose level in human tears with a detection concentration range of 0.03–100 μM and a detection limit of 0.406 nM. As expected, the novel appealing NIR-PEC glucose biosensor with multiple fascinating features will have a great potential for ultrasensitive glucose monitoring in metabolic diseases.

CRediT authorship contribution statement

Yue Tian: Methodology, Data curation, Formal analysis, Investigation, Writing – original draft. **Qingqiang Cui:** Methodology, Data curation. **Linlin Xu:** Data curation, Investigation. **Anxin Jiao:** Data curation, Investigation. **Hui Ma:** Data curation, Investigation. **Chang Wang:** Data curation, Investigation. **Mengya Zhang:** Data curation, Investigation. **Xuelin Wang:** Data curation, Investigation. **Shuang Li:** Supervision, Writing – review & editing, Funding acquisition. **Ming**

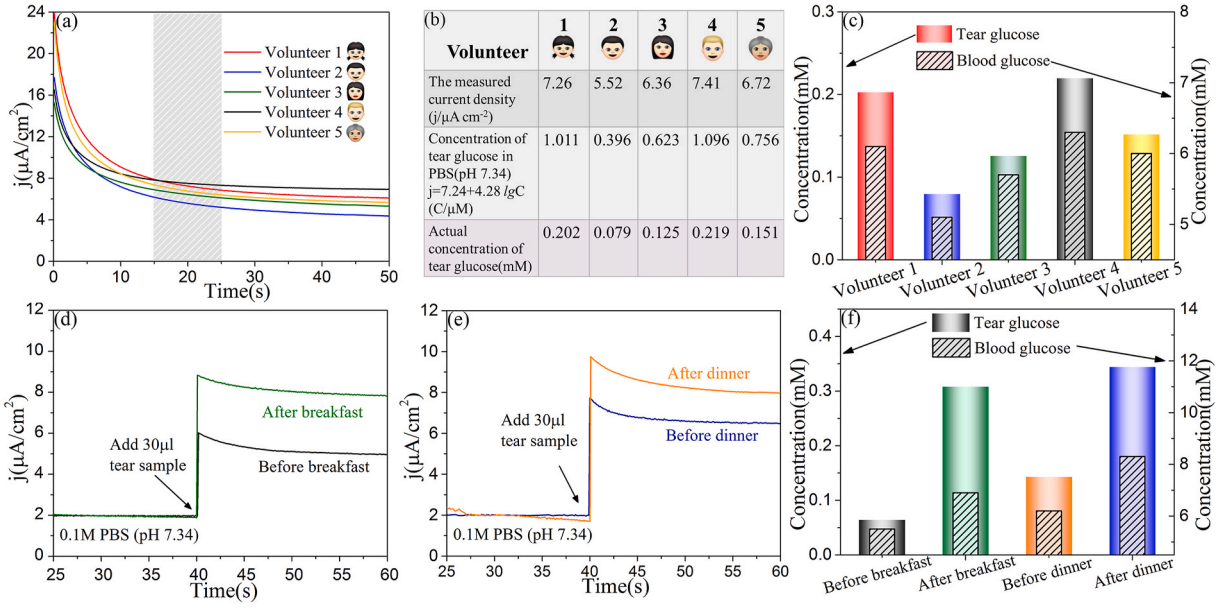

Fig. 6. (a) The amperometric response curves of human tears (diluted 200 times) from different volunteers. (b) The actual volunteers' tear glucose concentration and corresponding parameters. (c) Glucose concentration in tears (obtained by the sensor) and blood (measured by a blood glucose meter) of the five volunteers. The amperometric response curves of the variation of diluted human tears before and after (d) breakfast and (e) dinner. (f) Glucose concentration in tears (obtained by the sensor) and blood (measured by a blood glucose meter) of the volunteer before and after breakfast and dinner.

Chen: Supervision, Conceptualization, Writing – review & editing, Funding acquisition.

Declaration of competing interest

The authors declare that they have no known competing financial interests or personal relationships that could have appeared to influence the work reported in this paper.

Acknowledgments

This work was financially supported by the National Natural Science Foundation of China (NSFC) (Nos. 11905115 and 11575102), Shandong Jianzhu University XNBS Foundation (No. 1608) and Fundamental Research Fund of Shandong University (No. 2018JC022).

Appendix A. Supplementary data

Supplementary data to this article can be found online at https://doi.org/10.1016/j.bios.2021.113490.

References

Adriaenssens, A.E., et al., 2019. Cell Metabol. 30, 987–996.
Arakawa, T., et al., 2016. Biosens. Bioelectron. 84, 106–111.
Barman, I., et al., 2012. Anal. Chem. 84, 8149–8156.
Basu, D., et al., 2010. Electrochim. Acta 55, 5775–5779.
Cao, F., et al., 2020. Adv. Mater. 32, 1905362.
Chao, T.T., et al., 2019. ChemElectroChem 6, 289–303.
Chen, D.D., et al., 2020. Sensor. Actuator. B Chem. 323, 128692.
Chiu, W.T., et al., 2020. Sensor. Actuator. B Chem. 319, 128279.
Csapó, E., et al., 2012. Colloid. Surface. Physicochem. Eng. Aspect. 415, 281–287.
Girardi, L., et al., 2019. Surfaces 2, 41–53.
Grochowska, K., et al., 2017. Talanta 166, 207–214.
Han, J., et al., 2020. Biosens. Bioelectron. 170, 112675.
He, Y., et al., 2008. Adv. Mater. 20, 3416–3421.
Hsu, C.L., et al., 2017. J. Phys. Chem. B 121, 2931–2941.
Huang, X.Y., et al., 2016. Biosens. Bioelectron. 86, 530–535.
Iervolino, G., et al., 2018. Int. J. Hydrogen Energy 43, 2184–2196.
Jia, H., et al., 2016. Appl. Surf. Sci. 384, 58–64.
Karim, M.N., et al., 2018. Biosens. Bioelectron. 110, 8–15.
Koskun, Y., et al., 2018. Anal. Chim. Acta 1010, 37–43.
Kownacka, A.E., et al., 2018. Biomacromolecules 19, 4504–4511.
Li, D.W., et al., 2016. Electrochim. Acta 190, 852–861.
Li, H.J., et al., 2017. Biosens. Bioelectron. 91, 268–275.
Li, M., et al., 2021. Small, 2007179.
Li, W., et al., 2012. J. Mater. Chem. 22, 4025.
Linic, S., et al., 2015. Nat. Mater. 14, 567–576.
Liu, X.J., et al., 2019. Appl. Catal. B Environ. 249, 82–90.
Liu, X., et al., 2020. Chem. Commun. 56, 1784.
Lu, L., et al., 2018. Electrochim. Acta 185, 111.
Madriz, L., et al., 2020. Renew. Energy 152, 974–983.
Nantaphol, S., et al., 2017. Biosens. Bioelectron. 98, 76–82.
Peng, Y., et al., 2018. Nano Res. 11, 3222–3232.
Romeo, A., et al., 2018. Appl. Mater. Today 10, 133–141.
Salsali, A., Nathan, M., 2006. Am. J. Therapeut. 13, 349–361.
Toi, P.T., et al., 2019. ACS Appl. Mater. Interfaces 11, 10707–10717.
Wang, C., et al., 2017. ACS Nano 11, 5897–5905.
Wang, J., 2008. Chem. Rev. 108, 814–825.
Wang, L.F., et al., 2018. Biosens. Bioelectron. 111, 41–46.
Wang, L.F., et al., 2019. Biosens. Bioelectron. 142, 111577.
Wang, L.F., et al., 2020. Sensor. Actuator. B Chem. 304, 127330.
Wang, Y.X., 2014. J. Power Sources 245, 663–670.
Xie, Y.X., et al., 2020. Appl. Surf. Sci. 508, 145161.
Yamakoshi, K., et al., 2006. J. Biomed. Opt. 11, 054028.
Yang, J., et al., 2017. Sensor. Actuator. B Chem. 242, 728–735.
Yang, Y.L., et al., 2020. ACS Appl. Mater. Interfaces 12, 24845–24854.
Yao, H.F., et al., 2011. Biosens. Bioelectron. 26, 3290–3296.
Yoo, E.H., et al., 2010. Sensors 10, 4558–4576.
Yoshii, T., et al., 2019. J. Phys. Chem. C 123, 24575–24583.
Yoshii, T., et al., 2021. J. Catal. 394, 259–265.
Zhou, B.W., et al., 2016. Chem. Sci. 7, 463.